

## Research Article

<https://doi.org/10.1631/jzus.A2500674>

# Bond of rebar to crumb rubber concrete (CRC) under FRP-steel dual confinement: Failure mechanism and behavior modeling

Qiang LI<sup>1</sup>, Fangduo XIAO<sup>2✉</sup>, Shiwei LU<sup>3</sup>, Jizhong WANG<sup>4</sup>, Shikun CHEN<sup>2</sup>, Dongming YAN<sup>2✉</sup>

<sup>1</sup>College of Civil Engineering and Architecture, Zhejiang University of Water Resources and Electric Power, Hangzhou 310018, China

<sup>2</sup>College of Civil Engineering and Architecture, Zhejiang University, Hangzhou 310058, China

<sup>3</sup>School of Civil Engineering, Yantai University, Yantai 264005, China

<sup>4</sup>State Key Laboratory of Coastal and Offshore Engineering, Dalian University of Technology, Dalian 116024, China

**Abstract:** The replacement of traditional aggregates with recycled rubber in concrete is increasingly attractive, driven by sustainability-related considerations. Nevertheless, incorporating rubber particles alters both the microinterfacial characteristics and the macroscopic performance of concrete, which leads to the variation in bond behavior between rebar and rubberized concrete. Against this background, 42 central pull-out specimens were prepared for bond tests, and the impact of the rubber replacement ratio ( $\rho_{rv}$ ) on the bond behavior was investigated. Moreover, specimens with different confined conditions were designed to identify a reliable strengthening scheme for crumb rubber concrete (CRC) members. Test results show that when  $\rho_{rv}$  increases from 0 to 30%, the crack width of the splitting specimens decreases, but the bond strength deteriorates simultaneously. When  $\rho_{rv}$  increases to 40%, the specimens are subjected to splitting-pullout failure, and the deterioration of the bond strength can be alleviated. Specimens strengthened by fiber-reinforced polymer (FRP) and/or stirrups undergo pull-out failure and exhibit a bond strength at least 6.13% higher than that of their unstrengthened counterparts. Confinement enhances the bond strength of CRC specimens by up to 89.3%, beyond which further confinement induces no additional gains. By calibrating rubber-influenced parameters and the confinement critical effect, a mechanics-based model is established for predicting the bond strength of the CRC-bar interface. Finally, the stochasticity of the bond-slip response is simulated based on the assumption of multicomposite spring-friction units fracturing stochastically, and a continuous bond-slip model with high accuracy and an IAE below 10.47%, is proposed.

**Key words:** Crumb rubber concrete (CRC); Rubber replacement ratio ( $\rho_{rv}$ ); Bond strength model; Fiber-reinforced polymer (FRP)-steel confinement; Bond-slip model

## 1 Introduction

Numerous waste tires are produced annually (Azevedo et al., 2012), and the majority are disposed of in landfills (Ferdous et al., 2021). However, the long-term accumulation of waste rubber not only occupies land but also releases poisonous chemicals, causing pollution of soil and groundwater (Zhang et al., 2023). Furthermore, burning waste rubber can

produce carcinogens and greenhouse gases, aggravating air pollution and climate deterioration (Sienkiewicz et al., 2017). Consequently, it is of significance for sustainability to recycle and effectively utilize waste rubber. Many studies have reported crumb rubber concrete (CRC), in which rubber particles replace fine aggregates for engineering structures. This approach reutilizes waste rubber and simultaneously alleviates the consumption of river sand (Velegrakis et al., 2010; Raffoul et al., 2016; Guo et al., 2022).

Research shows that the ductility, wear resistance, and impact toughness of concrete can be improved after incorporating rubber particles, which contributes to the macroscopic static and seismic behavior of structural concrete (Abendeh et al., 2016;

✉ Fangduo XIAO, 12412091@zju.edu.cn

Dongming YAN, dmyan@zju.edu.cn

✉ Fangduo XIAO, <https://orcid.org/0009-0004-4959-1208>

Received Dec. 27, 2025; Revision accepted May 8, 2026;  
Crosschecked

Pham et al., 2020; Karunarathna et al., 2022). Therefore, CRC grants structural energy dissipation properties and enhanced deformation control, which has been increasingly applied in various large-scale infrastructure projects (Liu et al., 2025). Nevertheless, the hydrophobicity of rubber microscopically induces a highly porous interfacial transition zone (ITZ), while its low elastic modulus creates compressible voids, causing severe stress concentrations (Turatsinze and Garros, 2008; Gesoglu et al., 2015). Macroscopically, these defects accelerate microcrack initiation and coalescence under loading, fundamentally undermining the compressive strength (Mishra et al., 2026; Tan et al., 2026). This reduction, in turn, leads to a pronounced deterioration in the bond strength between the rebar and the CRC matrix (Xiao et al., 2026). The pull-out tests of Gesoglu et al. (2015) on CRC with a maximum rubber replacement ratio ( $\rho_{rv}$ ) of 30% indicate that the bond strength decreases up to 40% compared with that of normal concrete (NC). Similarly, Bompa and Elghazouli (2017) conducted bond tests of CRC with  $\rho_{rv}$  ranging from 0-60 % in 20 % increments and noted that the bond strength gradually decreases with increasing  $\rho_{rv}$ . An analogous observation is obtained by Bai et al. (2023)..

To compensate for the detrimental effect of rubber incorporation on bond strength, providing additional confinement has emerged as a promising approach. As indicated by the mechanics-based model of Xu et al. (2023), concrete dilation induced by rebar debonding activates passive confinement from external jackets or internal stirrups, generating additional radial stress at the bond interface to enhance bond performance. Traditionally, transverse reinforcement has been widely utilized to provide such well-confined conditions, with bond strength increasing significantly alongside the stirrup ratio (*fib*, 2010; Wang et al., 2020; Xiao et al., 2025a). Nevertheless, densely arranged internal stirrups can hinder concrete casting and fail to prevent visible surface cracks (Wang et al., 2024). Consequently, externally strengthening members with fiber-reinforced polymer (FRP) sheets to form an FRP-steel dual confinement system has become an attractive alternative. In practical engineering scenarios, this strengthening method is highly promising for the seismic retrofitting of bridge piers

and the upgrading of existing structural columns, where the superior energy dissipation of CRC and the high tensile strength of FRP can be synergistically utilized. As stated by Wang et al. (2023), specimens under FRP-steel dual confinement exhibit bond strengths at least 33.17% and 6.39% higher than unstrengthened and single-stirrup-strengthened specimens, respectively, while also displaying superior bond ductility. Despite these advantages, a critical confinement effect exists, leading to an upper bound for bond strength enhancement (Wang et al., 2024; Xiao et al., 2025a). Once crack development is fully restrained by confinement, further restraining efforts become superfluous and yield no additional bond capacity (Gambarova and Rosati, 1997; Wang et al., 2024). Given the inherently superior crack resistance and toughness of CRC, it is hypothesized that a reduced critical confinement level is required to reach this upper bound. Therefore, further clarification is urgently needed regarding the bond behavior between rebars and CRC under complex confinement conditions, specifically concerning the interplay between rubber content and the critical confinement threshold. As corresponding studies remain limited, addressing these issues is of vital importance for the reliable and economical design of CRC structures.

To gain insight into this issue, bond tests of steel bars to CRC were conducted. The rubber replacement ratio ranged from 0 to 40 % in 10 % increments. With respect to confinement, the specimens included unstrengthened, stirrup-strengthened, FRP-strengthened, and FRP-stirrup dual-strengthened cases. The program was designed to investigate the influence of these variables on the failure mode, bond-slip response, and bond strength. To predict bond strength under different confinement conditions, an analytical model was developed based on elastic-plastic mechanics, which offers better generalization than purely empirical closed-form formulas. Parameters influenced by the rubber replacement ratio and confinement conditions were calibrated against test data, enabling more accurate design predictions for the interfacial bond strength of CRC members. Furthermore, a new bond-slip model was proposed to facilitate finite-element simulation of the interfacial bond capacity between steel bars and CRC. Compared with *fib* (2010), the proposed model

achieves better agreement with measured bond-slip responses.

## 2 Experimental program

### 2.1 Specimen design

A total of 42 central pull-out specimens were tested. The influential factors considered in the program included the rubber replacement ratio, stirrup confinement, and FRP confinement. For the reliability of the test results, two duplicates were prepared for each specimen design. Inspired by the new structural configuration illustrated in Fig. 1, a 16-mm-diameter deformed bar was embedded along the central axis of a concrete cylinder. Its two ends were wrapped with PVC pipes to avoid stress concentration, resulting in a bonded length of 80 mm, as recommended by EN 10080 (2005). To avert potential cracks induced by thermal effects associated with excessive concrete cover, the ratio of concrete cover to bar diameter was designed as 2.94, consistent with practical construction details (Tang et al., 2015). In addition, a 6-mm-diameter plain bar was fabricated into a spiral with a spacing of 40 or 80 mm to serve as internal confinement for selected specimens.

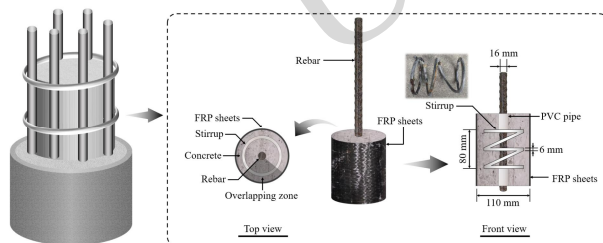


Fig. 1 Schematic of specimen

To ensure uniform dispersion of the rubber particles, a forced-action mixer was utilized to dry mix the aggregates and crumb rubber for 2 minutes to break up any potential clusters, followed by an additional 3 minutes of wet mixing after introducing cement and water. Concrete was poured vertically into molds. The load-end surface was polished using an angle grinder to ensure smoothness and close contact with the reaction frame during loading. After curing for 28 days, selected specimens were wrapped with one or two layers of FRP sheets, with a 115-mm overlap length to prevent jacket debonding.

Table S1 lists the specimen parameters and test results in detail. Specimens were named according to

the following principles: the first number represents  $\rho_{rv}$ ; S2 or S3 denotes stirrup spacing of 80 or 40 mm, respectively; and F1 or F2 indicates one or two layers of FRP sheets. For instance, 30-S2-F2 denotes a CRC specimen with  $\rho_{rv}$  of 30% strengthened by 80-mm-spacing stirrups and two-layer FRP sheets.

### 2.2 Material properties

The 42.5-grade ordinary Portland cement was used for all mix proportions. As per ASTM C33/C33 M-18 (2018), well-graded aggregates with nominal sizes ranging from 5 to 20 mm were adopted. In accordance with GB/T 14684 (2011), river sand with a maximum nominal size, fineness modulus, and density of 5 mm, 2.6, and 2650 kg/m<sup>3</sup>, respectively, was adopted for fine aggregate. In CRC mixtures, a portion of sand was replaced by rubber particles at volume ratios of 10 %, 20 %, 30 %, and 40 %. This specific range was selected to capture the transition of bond behavior while avoiding the excessive mechanical degradation typically observed beyond a 40% replacement. The rubber particle size ranged from 0.25 to 4 mm, which matches the gradation of the replaced sand to minimize strength loss, with a density of 925 kg/m<sup>3</sup>, consistent with relevant literature (Bompa and Elghazouli, 2017; Romanazzi et al., 2021; Lu et al., 2024). The mix proportions of the concrete are summarized in Table 1, and the rubber particle gradation ratios were designed as 2.25:5.62:10.11:4.49 to achieve a distribution similar to that of the sand, as shown in Fig. 2 (BSI 1992). For each mix proportion, three duplicate 100-mm cubes were prepared to determine the compressive strength ( $f_{cu}$ ), as shown in Fig. 3. It is evident that  $f_{cu}$  decreases with increasing  $\rho_{rv}$ , which is consistent with the observation of Liu et al. (2023).

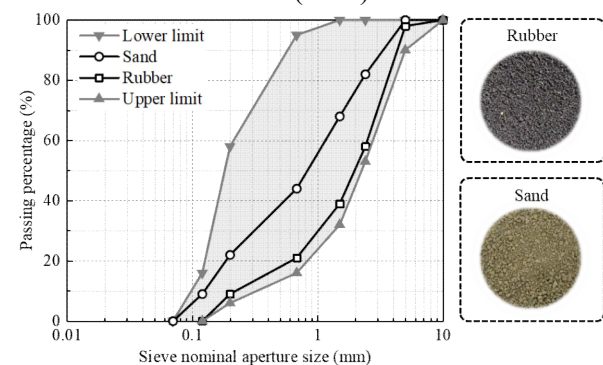




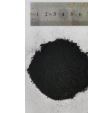




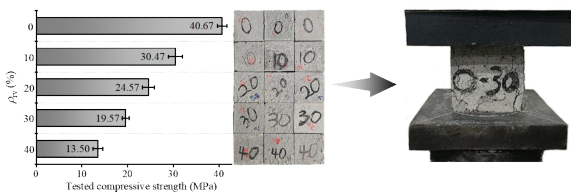


Fig. 2 Particle size distributions of fine aggregates

**Table 1 Mix proportions of concrete (kg/m<sup>3</sup>)**

Category	Cement	Fly ash	Gravel	Sand	Rubber A	Rubber B	Rubber C	Rubber D	Water
Photograph									
$\rho_{rv}=0\%$	373	50	1273	637	0	0	0	0	170
$\rho_{rv}=10\%$	373	50	1273	573	2.25	5.62	10.11	4.49	170
$\rho_{rv}=20\%$	373	50	1273	510	4.49	11.24	20.23	8.99	170
$\rho_{rv}=30\%$	373	50	1273	446	6.74	16.85	30.34	13.48	170
$\rho_{rv}=40\%$	373	50	1273	382	8.99	22.47	40.45	17.98	170



**Fig. 3 Test results of concrete strength**

A deformed rebar with a nominal diameter ( $d$ ) of 16 mm was used, and the corresponding surface geometries were measured using a Vernier caliper, as shown in Fig. 4. In accordance with GB/T 228.1 (2010), the tensile stress–strain curves of the reinforcement were obtained (Fig. 4).

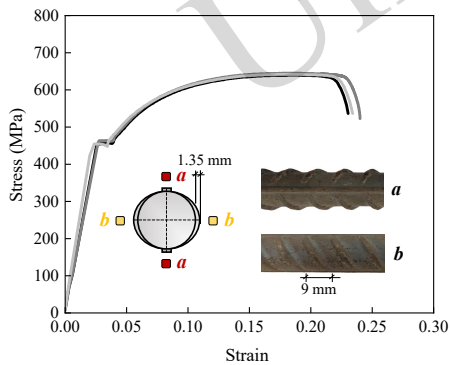


**Fig. 4 Stress-strain curve and surface geometry of reinforcement**

As per the manufacturer’s information, the FRP parameters were recorded as follows: areal weight= 299 g/m<sup>2</sup>; nominal thickness= 0.167 mm; tensile strength= 3739 MPa; elastic modulus= 240 GPa; ultimate rupture strain= 0.0171. Additionally, the interfacial bond strength between the concrete and FRP sheets was 5.4 MPa in accordance with GB/T 50728 (2011).

**2.3 Test setup**

The central pull-out tests were conducted via a 200 kN servo-controlled test machine. As per Xiao et al. (2025b), the displacement-controlled rate was 1 mm/min. As illustrated in Fig. 5, the load-end surface of the concrete was in close contact with the homemade frame, while the load-end reinforcement was clamped by a chuck. The applied force was measured by a load cell. A pair of linear variable displacement transducers (LVDTs) fixed on the steel frame served to capture the load-end slip, and an LVDT fixed on the magnetic base was used to collect the free-end slip.

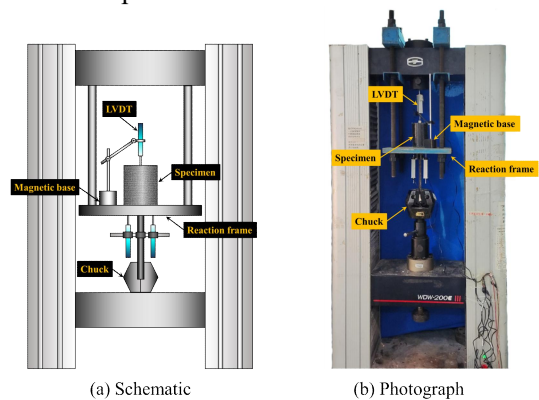


**Fig. 5 Test setup**

**3 Test results**

**3.1 Bond-slip response and failure mode**

As recommended by RILEM (1983), the embedment length of  $5d$  allows approximately uniform stress along the bonded zone. Thus, Eq. (1) was used to determine the bond stress  $\tau$ . Considering rebar deformation between the load-end LVDTs and the bonded region, Eq. (2) was adopted to determine nominal slip  $s$  (Xiao et al., 2025b).

$$\tau = \frac{F}{\pi dl} \quad (1)$$

$$s = \frac{1}{2} \left( s_1 + s_f - \frac{4Fl_a}{\pi d^2 E_s} \right) \quad (2)$$

where  $F$  is the pull-out load;  $l$  is the embedment length;  $s_1$  is the load-end slip;  $s_f$  is the free-end slip;  $E_s$  is the reinforcement elastic modulus; and  $l_a$  is the distance between the load-end LVDTs and bonded region.

Fig. 6 illustrates the bond-slip curves of the unstrengthened specimens, most of which exhibit only the prepeak branch due to splitting failure. In this case, circumferential stress exceeds the tensile capacity of concrete and induces multiple cracks, resulting in loss of confinement to the core concrete. Therefore, a postpeak branch cannot develop under splitting failure, consistent with the bond-slip response under insufficient confinement reported in *fib* (2010). Moreover,  $\rho_{rv}$  plays an important role in the bond-slip behavior of unstrengthened specimens: the initial bond stiffness decreases as  $\rho_{rv}$  increases. Wang et al. (2020) reported that the initial bond-slip behavior is governed by chemical adhesion. However, incorporating rubber particles reduces the area of cement paste in contact with the steel surface, indirectly weakening the chemical adhesion.

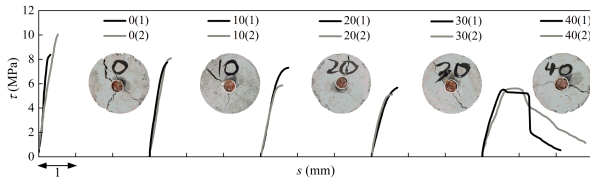
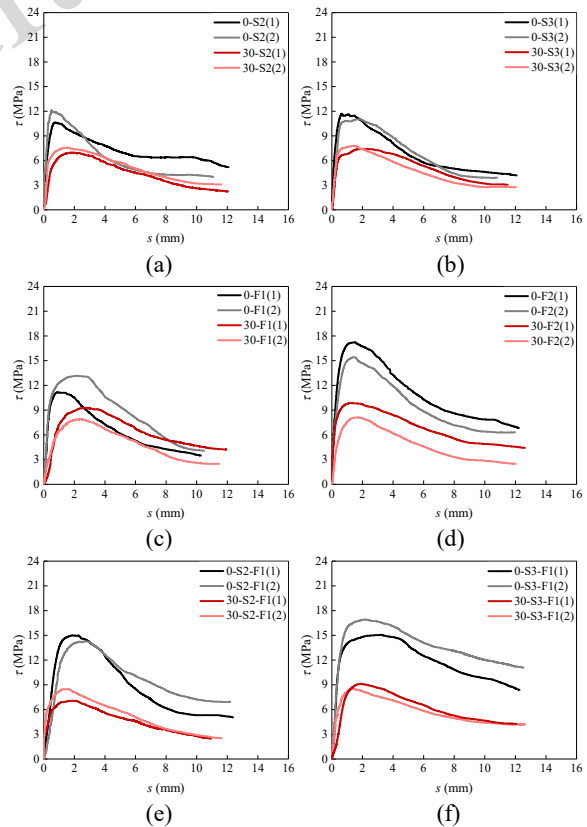


**Fig. 6 Bond-slip curves and failure phenomena of unstrengthened specimens**

Additionally, the macroscopic failure is significantly influenced by  $\rho_{rv}$ . For NC specimens, pronounced brittleness is evidenced by more than three visible cracks on the free-end surface. With increasing  $\rho_{rv}$ , cracking is alleviated. Specifically, for  $\rho_{rv} = 10\%$  and  $20\%$ , three cracks remained visible, but their widths were significantly smaller than those in NC. When  $\rho_{rv}$  increased to  $30\%$ , only two visible cracks propagated to the concrete cover edge, although splitting failure still occurred. When  $\rho_{rv}$  further increased to  $40\%$ , the failure mode changed into pull-out failure with splitting. In this case, the concrete matrix still provides weak confinement to

the bond interface, and a ductile postpeak segment can be observed. This is because crack tips are blunted by rubber particles, restraining crack propagation (Bai et al., 2023).

All specimens strengthened by confinement components underwent pull-out failure, and typical ductile bond-slip curves were obtained (Fig. 7), featuring a postpeak branch with soft unloading stiffness. This indicates that crack-induced concrete dilation activates the mechanical response of stirrups or FRP, which in turn provides confinement to the core region and contributes to ductile bond-slip behavior. However, the unloading stiffness of CRC specimens is smaller than that of NC specimens under identical confinement conditions. This may be attributed to the porous structure of CRC arising from the weak rubber-matrix interface, which allows greater energy dissipation (Ganjian et al., 2009; Hall and Najim, 2014).



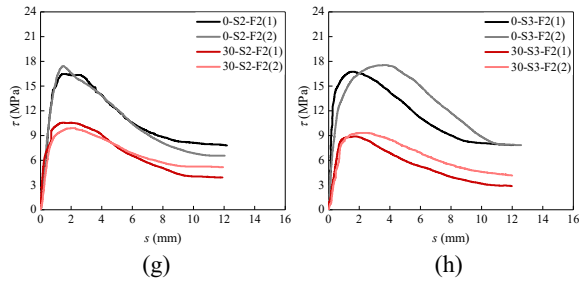


Fig. 7 Bond-slip curves of strengthened specimens

Note that a certain degree of variability exists between the duplicate specimens. This is attributed to the inherent heterogeneity of the concrete matrix. The random spatial distribution of aggregates near the rebar ribs leads to localized variations in the mechanical interlocking force. Furthermore, the highly sensitive nature of the concrete failure mechanism inherently contributes to the observed scatter in bond strength.

### 3.2 Factors influencing bond strength

#### 3.2.1 Impact of rubber content

Fig. 8 shows the influence of the rubber content on the bond strength of the unstrengthened specimens. The bond strength decreases as  $\rho_{rv}$  increases from 0 to 30%, which is expected due to the reduction in  $f_{cu}$ . Notably, the bond strength of specimen 40 is higher than that of specimen 30, although its  $f_{cu}$  is only 68.98% of the latter. This can be attributed to the different failure modes. For specimen 40, which underwent pull-out failure with splitting, the partially intact concrete matrix enables continued interaction between rebar and concrete, leading to more fully developed bond stress than in splitting failure. This finding suggests that a critical  $\rho_{rv}$  may result in a balance between bond strength and ductility for the anchorage design of CRC members.

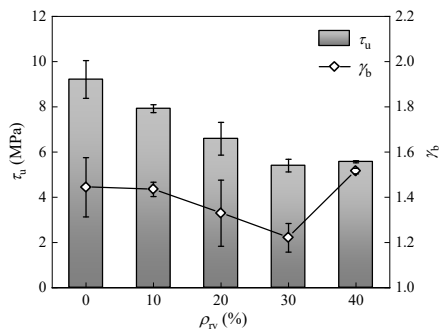


Fig. 8 Influence of  $\rho_{rv}$  on bond strength of unstrengthened specimens

As recommended by *fib* (2010), the interfacial bond strength can be normalized to exclude the influence of compressive strength using the bond coefficient  $\gamma_b = \tau_u / (f_{cu})^{0.5}$ . Fig. 8 shows that  $\gamma_b$  gradually decreases as  $\rho_{rv}$  increases from 0 to 30%, indicating that the normalized bond capacity of CRC is lower than that of NC. This reduction may be associated with changes in tensile strength that alter crack inclination in front of steel ribs and reduce the concrete-bar wedge effect. Alternatively, rubber particles with a low elastic modulus and high Poisson's ratio may modify frictional behavior at the rebar-CRC interface (Topçu, 1995; Bompa and Elghazouli, 2017).

#### 3.2.2 Impact of additional confinement

Fig. 9 shows the influence of confinement conditions on bond strength. As shown in Fig. 9 (a), confinement significantly increases the bond strength. For example, the bond strength of strengthened NC and CRC specimens is 23.24% and 34.07% higher than that of their unstrengthened counterparts, respectively. The effect of stirrups/FRP can be attributed to (a) increased radial pressure at the bond interface and (b) restrained cracking, which ensures sustained interaction between rebar and surrounding concrete (Xu et al., 2023; Xiao et al., 2025a). FRP generally outperforms stirrups because it confines a larger region (Xu et al., 2023), and a similar conclusion is found by Wang et al. (2023).

In addition, it is found that reducing stirrup spacing plays a negligible role in bond strength. For instance, the bond strength of specimen 30-S3 is merely 4.97% higher than that of specimen 30-S2, and the bond strength between specimen 0-S3 and specimen 0-S2 nearly coincides. In contrast, the increase in the number of FRP layers heavily improves the bond strength of the NC specimens, as the bond strength of specimen 0-F2 is 34.24% higher than that of its one-layer FRP-strengthened counterpart. Interestingly, the bond strength of the CRC specimen confined by two layers of FRP is only 4.78% higher than that of specimen 30-F1. This may be attributed to the deviation in fracture energy between the two types of concrete. The superior crack resistance of CRC induces additional FRP confinement redundancy. Similar phenomena are also

observed for specimens strengthened by dual confinement. It is apparent that the bond strength of NC specimens is enhanced by improving the confinement level. For example, in terms of the specimens with 40-mm-spacing stirrups, the bond strength is 11.35 MPa, 15.95 MPa, and 17.13 MPa when the number of layers of FRP sheets increases from 0 to 2. Alternatively, for specimens wrapped with single-layer FRP, the bond strength ratios of specimens 0-S2-F1 and 0-S3-F1 to 0-F1 are 1.20 and 1.31, respectively. However, the bond strength varies little for CRC specimens under different confinement levels. It can be inferred that the bond strength of well-confined CRC members is heavily dominated by the interfacial characteristics rather than the additional confinement. This finding indicates that the mix proportion of CRC should be emphasized in anchorage design, enabling potential savings in confinement cost.

Fig. 9 (b) compares CRC and NC using  $\gamma_b$ . The majority of test results show that the  $\gamma_b$  of NC remains superior to that of CRC regardless of confinement conditions. Therefore, an additional safety coefficient is required in CRC structural design, even when confinement is provided, considering the strength degradation caused by rubber incorporation.

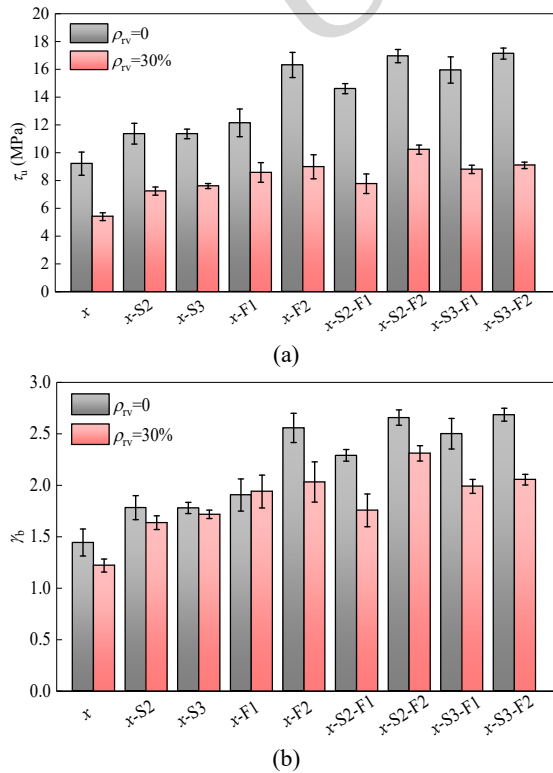
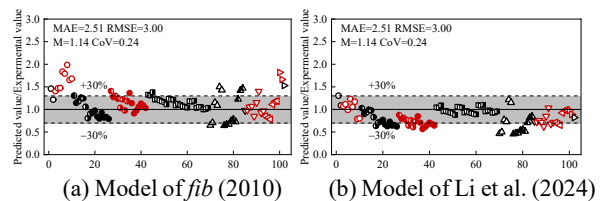


Fig. 9 Influence of different confinement conditions on bond strength

#### 4 Analytical bond strength model

##### 4.1 Performance evaluation of existing models

In accordance with the following criteria, a database from relevant studies was assembled from relevant studies (Choi et al., 2014; Gao et al., 2019; Li et al., 2020; Kammash et al., 2022; Bai et al., 2023): (a) only specimens cast with NC or CRC were covered, and other types of concrete, e.g., seawater sea-sand concrete, geopolymer concrete, and fiber-reinforced concrete, were excluded; (b) only the bond behavior of deformed carbon steel bars was compared; and (c) with respect to the strengthened specimens, only the device of stirrups or FRP was considered. Table S2 lists more details of the database. By comparing the experimental data to the theoretical predictions of *fib* (2010), the notable nonconservative predictions for the CRC specimens are inspected from Fig. 10 (a). Consequently, *fib* (2010) may be inadequate for the anchorage design of CRC structures due to differences in interfacial mechanisms. In this case, several novel models were developed by directly fitting the bond test results of CRC specimens, e.g., Li et al. (2024) and Chen et al. (2023). However, these closed-form formulas cannot take comprehensive factors into consideration, leading to poor generalization [Fig. 10 (b) and (c)], as reflected by undesirable statistical indicators, i.e., mean absolute error (MAE), root mean squared error (RMSE), mean (M), and coefficient of variation (CoV). This may be caused by the fact that such empirical models are developed based on the variables designed in the experiment, whereas the factors outside of the predesign cannot be captured. Therefore, analytical modeling for the interfacial bond strength between rebar and CRC based on physical assumptions is needed due to its excellent extrapolation for the scenarios outside of the source database (Zhang et al., 2019; Xu and Yan, 2023; Xu et al., 2023).



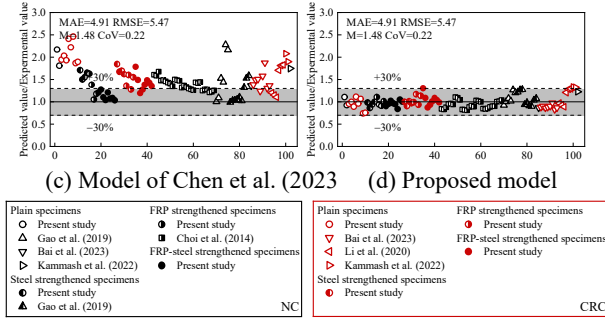


Fig. 10 Predicted accuracy of bond strength models

## 4.2 Mechanics-based model

### 4.2.1 Radial stress

As shown in Fig. 11, the fictitious crack assumption defines a double-cylinder model consisting of an inner plastic region and outer elastic region (Li et al., 2021), where  $r_s$ ,  $r_{cr}$ , and  $r_e$  represent the rebar radius, fictitious crack radius and specimen radius, respectively. The fictitious crack model sets the tangential stress at the crack tips equal to the concrete tensile strength ( $f_t$ ), resulting in constant concrete strain ( $\varepsilon_{cr}$ ) within the plastic region. According to the equilibrium of deformation, the crack width ( $w_c$ ) evolves linearly along the radial direction and is expressed by Eq. (3) (Xu and Yan, 2023; Xu et al., 2023).

$$w_c = \frac{2\pi\varepsilon_{cr}}{N}(r_{cr} - r) = \frac{2\pi f_t}{NE_c}(r_{cr} - r) \quad (3)$$

where,  $r_{cr}$  stands for the fictitious crack radius,  $E_c$  denotes the elastic modulus of concrete, and  $N$  is the crack number.

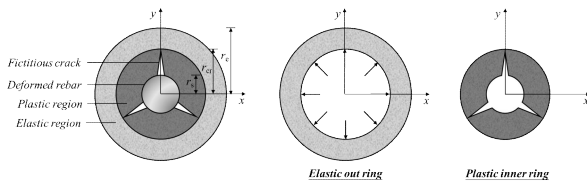


Fig. 11 Fictitious crack model

The cohesion ( $\sigma_{w,r}$ ) within cracks provides bridging traction, which governs the radial stress on the bond interface from the inner plastic region. In this sense, a corresponding analytical solution is obtained using the exponential constitutive  $\sigma_{w,r}-w_c$  model reported by Reinhardt et al. (1986). On the other hand, the interfacial radial stress from the outer elastic region is equilibrated with the uniform

pressure at the inner wall of the elastic cylinder, which is inspired by the hydraulic pressure analogy. Thus, the radial stress ( $\sigma_1$ ) provided by the concrete cover can be calculated by Eq. (4).

$$\sigma_1 = f_t \frac{r_{cr} r_e^2 - r_{cr}^2}{r_s r_e^2 + r_{cr}^2} + \frac{\int_{r_s}^{r_{cr}} \sigma_{w,r} dr}{r_s} \quad (4)$$

The contribution of stirrups/FRP arises because crack-induced dilation causes tensile deformation in these components, activating confinement and increasing radial stress at the bond interface. The radial stress ( $\sigma_2$ ) provided by stirrups/FRP is expressed by Eq. (5), where the strain of the confinement component is determined by Eqs. (6) and (7) for the cases without and with crack penetration at the component location, respectively.

$$\sigma_2 = \frac{E_{st}\varepsilon_{st}A_{st}}{2rl} + \frac{E_f\varepsilon_fA_f}{2rl} \quad (5)$$

$$\varepsilon_{st} = \varepsilon_{cr} \frac{r_e^2 + r_{st}^2}{r_e^2 + r_{cr}^2} \frac{r_{cr}^2}{r_{st}^2} \quad (6a)$$

$$\varepsilon_f = \varepsilon_{cr} \frac{2r_{cr}^2}{r_e^2 + r_{cr}^2} \quad (6b)$$

$$\varepsilon_{st} = \frac{Nw_{st} + 2\pi r_{st}\varepsilon_{cr}}{2\pi r_{st}} \quad (7a)$$

$$\varepsilon_f = \frac{Nw_f + 2\pi r_e\varepsilon_{cr}}{2\pi r_e} \quad (7b)$$

where  $E_{st}$  and  $E_f$  represent the elastic modulus of the stirrup and FRP, respectively;  $A_{st}$  and  $A_f$  denote the cross-sectional area of the stirrup and FRP, respectively;  $r_{st}$  is the radial coordinate where the stirrup is located; and  $w_{st}$  and  $w_f$  stand for the crack width at  $r=r_{st}$  and  $r=r_e$ , respectively.

By increasing  $r_{cr}$  with a given step length until the calculated radial stress computed at the current  $r_{cr}$  is no larger than that at the previous  $r_{cr}$ , the governing radial stress for ultimate bond stress is obtained.

### 4.2.2 Bond stress

Existing analytical models indicate that the bond stress comprises two components, i.e., the concrete-to-concrete wedge effect and concrete-to-steel friction (Choi and Lee, 2002; Zhang et al., 2019; Xu et al., 2022). The former is associated with crushed concrete with an inclined failure surface ahead of the steel ribs. The latter is controlled by the global friction between the steel bar and concrete within a bond unit. In this sense, the bond stress can

be obtained by Eq. (8), in which the resultant radial stress is considered the dominant factor.

$$\tau = (\sigma_1 + \sigma_2) \left[ \frac{\sin \alpha + \mu_1 \cos \alpha \frac{2\pi r_s h_r \cot \alpha}{\cos \alpha - \mu_1 \sin \alpha} \frac{2\pi r_s (s_c + s_r)}{2\pi r_s (s_c + s_r)}}{\mu_2 \frac{2\pi r_s s_c + \mu_2 (2\pi r_s + 2\pi h_r) s_r}{2\pi r_s (s_c + s_r)}} \right] \quad (8)$$

where  $\mu_1$ = concrete-to-concrete friction coefficient;  $\mu_2$ = concrete-to-steel friction coefficient;  $s_c$ = rib spacing between two adjacent ribs;  $s_r$ = rib width; and  $h_r$ = rib height.

However, compared with NC specimens, the inferior  $\gamma_b$  as well as the critical effect of confinement should both be carefully considered for the bond strength model of CRC specimens. First, based on regression analysis, a coefficient  $\xi_r$  dependent on  $\rho_{rv}$  is proposed to capture the impact of rubber on the macroscopic bond strength [see Eq. (9)].

$$\xi_r = \exp(-0.342\rho_{rv}) \quad (9)$$

In addition, since the inherent crack resistance of CRC can render additional confinement redundant, the bond strength model is further improved using Eq. (10) by incorporating the critical  $\sigma_2$ .

$$\tau = \begin{cases} (\sigma_1 + \sigma_2) \left[ \frac{\sin \alpha + \mu_1 \cos \alpha \frac{2\pi r_s h_r \cot \alpha}{\cos \alpha - \mu_1 \sin \alpha} \frac{2\pi r_s (s_c + s_r)}{2\pi r_s (s_c + s_r)}}{\mu_2 \frac{2\pi r_s s_c + \mu_2 (2\pi r_s + 2\pi h_r) s_r}{2\pi r_s (s_c + s_r)}} \right] \xi_r & \sigma_2 / f_t \leq 3.76 \\ (\sigma_1 + 3.76f_t) \left[ \frac{\sin \alpha + \mu_1 \cos \alpha \frac{2\pi r_s h_r \cot \alpha}{\cos \alpha - \mu_1 \sin \alpha} \frac{2\pi r_s (s_c + s_r)}{2\pi r_s (s_c + s_r)}}{\mu_2 \frac{2\pi r_s s_c + \mu_2 (2\pi r_s + 2\pi h_r) s_r}{2\pi r_s (s_c + s_r)}} \right] \xi_r & \sigma_2 / f_t > 3.76 \end{cases} \quad (10)$$

Other material parameters within the bond strength model are summarized in Table S3 in accordance with existing reports (Reinhardt et al., 1986; GB/T 1499.2 2007; fib 2010; Bompa and Elghazouli, 2017; ASTM 2018 Ka et al., 2018; Zhao and Zhu, 2018). As illustrated in Fig. 10 (d), the proposed model outperforms existing models in terms of prediction accuracy, accompanied by desirable statistical indicators.

## 5 Continuous bond-slip model

### 5.1 Theoretical modeling

The macroscopic response induced by rebar debonding, in fact, is the comprehensive manifestation of the stochastically distributed microscopic damage, covering microcracks, voids, and defects (Huang et al., 2019a). Due to the intrinsic heterogeneity of concrete materials, the bond-slip responses among duplicate specimens still present deviations, as shown in Fig. 12 (a). To phenomenologically simulate the stochasticity of the bond-slip response, the concrete-bar bond is described by the behavior of  $N$  spring-friction units with duplicate stiffness  $K$  [Fig. 12 (b)]. The assumed spring element follows linear elasticity up to a critical tensile extension  $\Delta$  and services for transmitting the bond stress. However, the bond stress will be transferred to the friction element to bear once the spring element fractures. Thus, the bond-slip response induced by a bond unit is depicted in Fig. 12 (c), which can be expressed by Eq. (11). By giving different mechanics parameters to each spring element, they will be subjected to stochastic fracture, resulting in the rewritten expression of the bond-slip response determined by a bond unit [see Eq. (12)]. The fracture of multiple springs results in macroscopic nonlinearity, a significant characteristic of the bond-slip response (Huang et al., 2019a), as illustrated in Fig. 12 (d).

$$\tau_i = \begin{cases} Ks & s \leq \Delta \\ \tau_f & s > \Delta \end{cases} \quad (11)$$

$$\tau_i = [1 - H(s - \Delta)]Ks + H(s - \Delta)\tau_f \quad (12)$$

where  $\tau_i$  represents the bond stress of the  $i$ th bond unit, and  $\tau_f$  denotes the residual bond stress determined by the friction element.

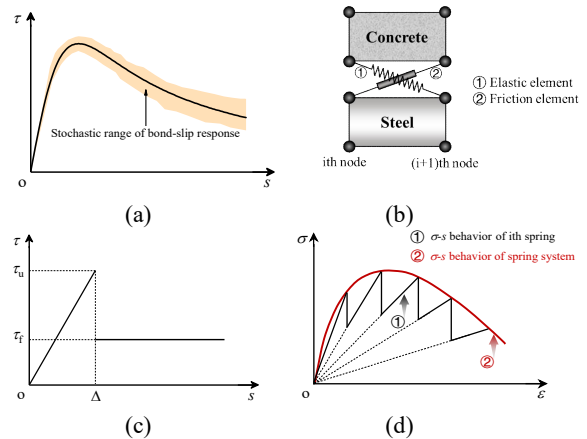


Fig. 12 Manifestation of the stochasticity and nonlinearity of bond-slip response

As depicted in Eq. (13), the stochastic fracture of the spring system composited by  $N$  units can be expressed by a damage variable  $D$ , and hence, the macroscopic bond-slip response is written as Eq. (14).

$$D = \frac{\sum_{i=1}^N H(s-\Delta)}{N} \quad (13)$$

$$\tau = (1-D)Ks + D\tau_f \quad (14)$$

The reasonable definition of  $D$  is of great significance to ensure the continuity of the bond-slip model because the joint selection of the segmented model significantly affects the calculated results of the finite-element capacity and causes inconsistencies near joints, e.g., *fib* (2010). To address this issue, the Weibull density function shown in Eq. (15) is adopted due to its suitability for quasibrittle fracture. Accordingly,  $D$  is expressed by Eq. (16) and accords with the mandatory constraints, i.e.,  $0 \leq D(s) \leq 1$ ,  $D(s=0)=0$ , and  $dD(s) \geq 0$  (Huang et al., 2019b).

$$f(\delta) = \frac{k}{\lambda} \left(\frac{\delta}{\lambda}\right)^{k-1} \exp\left(-\frac{\delta^k}{\lambda^k}\right) \quad (15)$$

$$D = \int_0^s f(\delta) d\delta = \frac{k}{\lambda} \left(\frac{\delta}{\lambda}\right)^{k-1} \exp\left(-\frac{\delta^k}{\lambda^k}\right) d\delta = 1 - \exp\left(-\frac{s^k}{\lambda^k}\right) \quad (16)$$

where  $\delta$  is the stochastic variable for describing spring fracture and  $k$  and  $\lambda$  are the shape and scale parameters of the Weibull distribution, respectively (Xiao et al., 2025a).

## 5.2 Parameter calibration for bond-slip model

### 5.2.1 Residual bond behavior

Zhao and Zhu (2018) defined that the residual behavior is achieved as the slip arrives at  $s_c + s_r$ . In this sense, the ratios ( $\psi$ ) of residual bond stress to ultimate bond stress are presented in Fig. 13 (a) and (b) for NC and CRC specimens, which are proposed as 0.48 and 0.46, respectively.

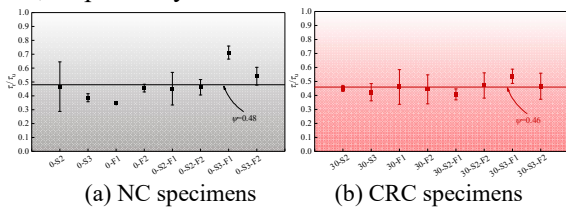


Fig. 13 Calibration of residual bond stress

### 5.2.2 Spring stiffness

The spring stiffness  $K$  is inherently determined by the material and structural parameters of the specimens, despite the loading conditions. Unfortunately, the assumed parameter  $K$  fails to be obtained by means of experiments, and the corresponding analytical determination is absent in existing studies. As a result, the bond strength calculated via the foregoing analytical model will be employed to invert it hereinafter.

As depicted in Eq. (17), the ultimate bond stress can be expressed in another form. In addition,  $\delta\tau_u/\delta s_u = 0$  is noted near the ultimate state due to the continuity of the proposed bond-slip model. By inputting this condition into Eq. (17), the value of  $K$  can be easily determined.

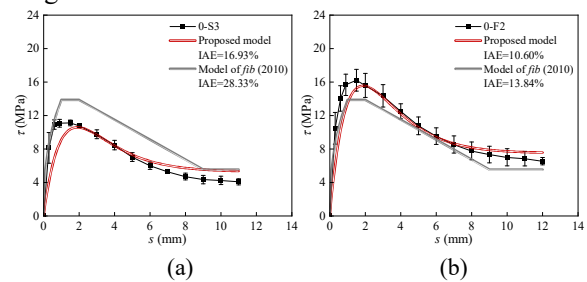
$$\tau_u = \exp\left(-\frac{s_u^k}{\lambda^k}\right) K s_u + \left[1 - \exp\left(-\frac{s_u^k}{\lambda^k}\right)\right] \psi \tau_u \quad (17)$$

where  $s_u$  denotes the slip under  $\tau_u$ .

## 5.3 Model validation

Fig. 14 shows the comparisons of the experimental bond-slip curves to the theoretical predictions of the proposed model as well as the *fib* (2010) model, while the integral absolute error (IAE) is used to quantify their accuracy. In contrast, the proposed model achieves superior agreement with the stochastic range of the bond-slip response, and the corresponding IAE for all cases is less than 20%. Although an anomalous phenomenon is inspected in Fig. 14 (i), the accuracy of the proposed model, i.e., IAE= 10.47%, is still acceptable.

To facilitate practical engineering applications, the proposed continuous bond slip model can be incorporated into finite element analysis. This integration enables the accurate simulation of the nonlinear macroscopic behavior and the superior energy dissipation of confined members, thereby providing a reliable numerical tool for the seismic design of CRC structures.



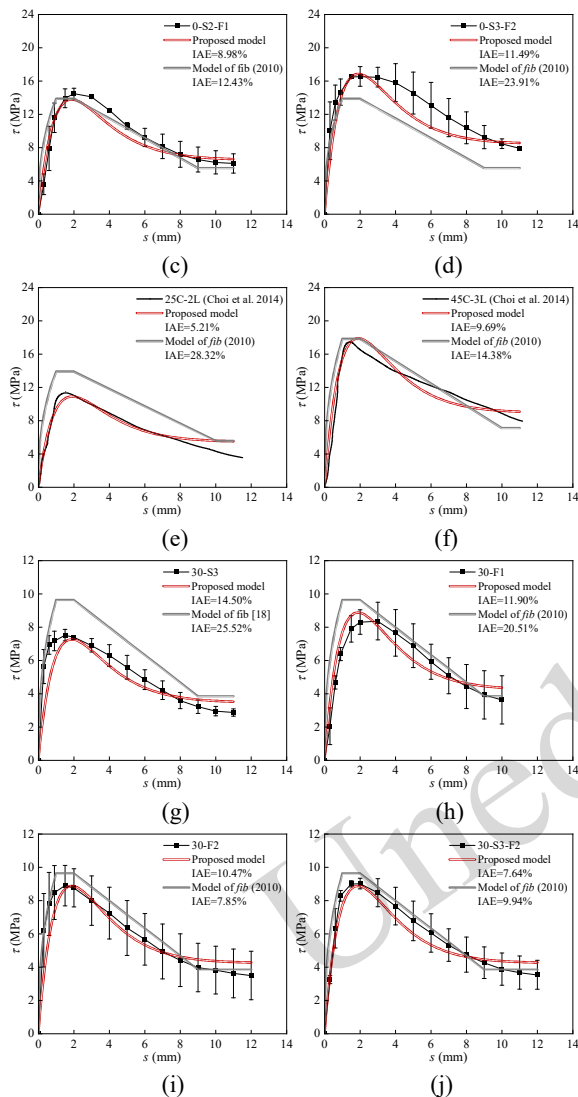


Fig. 14 Comparisons of theoretical predictions to experimental results

## 6 Conclusions

This novel evolution law of bond behavior revealed in the present study differed from those of previous research because the coupling effect of the rubber replacement ratio and additional confinement was comprehensively discussed. The following conclusions are meaningful for the structural design of sustainable engineering:

(1) The increase in rubber content significantly degrades the bond strength of unstrengthened specimens but contributes to the postponement of the development of concrete cracks. As  $\rho_{TV}$  increases to 40 %, the brittle splitting failure of unstrengthened specimens tends to transform into pull-out failure

with splitting, while the bond strength degradation is conspicuously alleviated, which inspires a potential  $\rho_{TV}$  to achieve the optimal bond strength and ductility synchronously for CRC member design.

(2) Compared with the unstrengthened cases, the use of stirrup/FRP confinement is apparent to improve the bond behavior regardless of the concrete type. Nevertheless, the increase in confinement level contributes to the bond strength of NC specimens but plays a negligible role in that of CRC specimens. This finding proposes that the usage of confinement devices should be considered for the anchorage design of CRC members.

(3) An analytical model based on fictitious crack theory is proposed for predicting the bond strength of steel bars to CRC, which is further improved by taking the degradation coefficient  $\xi_r$  and the critical confinement effect into consideration. The composite spring-friction system is assumed to establish a continuous bond-slip model. The high predicted accuracy, as well as the stochasticity and nonlinearity of the bond-slip response, is synchronously revealed.

Nevertheless, the evolution law of bond behavior revealed in this study is only accepted for quasistatic conditions, failing to reflect the transient responses of earthquake-stricken structures. Furthermore, investigating the coupling effects of steel corrosion and external confinement on the bond degradation mechanisms of CRC members is needed. Finally, the proposed coefficient  $\xi_r$  in the present form cannot manifest the threshold effect of the rubber replacement ratio, which should be determined based on further bond tests

## Acknowledgments

This work is supported by the Zhejiang Provincial Natural Science Foundation of China under Grant No.LTGG23E080008. We thank Mr. Chenkang LI and Mr. Weiqi SUN (State Key Laboratory of Coastal and Offshore Engineering, Dalian University of Technology, China) for their generous assistance in the experimental work.

## Author contributions

Qiang LI designed the research. Shiwei LU and Jizhong WANG processed the corresponding data. Fangduo XIAO wrote the first draft of the manuscript. Shikun CHEN helped to organize the manuscript. Dongming YAN revised and edited the final version.

## Conflict of interest

Qiang LI, Fangduo XIAO, Shiwei LU, Jizhong WANG, Shikun CHEN, and Dongming YAN declare that they have no conflict of interest.

### Declaration on the use of generative AI tools

As generative AI tools have become increasingly popular, authors must declare whether they have used these tools during the preparation of the manuscript.

### Data availability

The data that support the findings of this study are available from the corresponding author upon reasonable request.

### References

- Azevedo F, Pacheco-Torgal F, Jesus C, et al., 2012. Properties and durability of HPC with tyre rubber wastes. *Construction and Building Materials*, 34:186-191.
- Abendeh R, Ahmad HS, Hunaiti YM, 2016. Experimental studies on the behavior of concrete-filled steel tubes incorporating crumb rubber. *Journal of Constructional Steel Research*, 122:251-260.
- ASTM, 2018. ASTM C33/C33M-18: *Standard Specification for Concrete Aggregates*. ASTM International, USA.
- Bai YH, Zhang DY, Chen K, et al., 2023. Bonding properties of rubber concrete and deformed steel bars: Experimental and numerical study. *Construction and Building Materials*, 383:131416.
- Bompa DV, Elghazouli AY, 2017. Bond-slip response of deformed bars in rubberised concrete. *Construction and Building Materials*, 154:884-898.
- BSI, 1992. BS 882: *Specification for Aggregates from Natural Sources for Concrete*. British Standards Institution, London.
- CEN, 2005. EN 10080: *Steel for the Reinforcement of Concrete-Weldable Reinforcing Steel*. European Committee for Standardization, Brussels.
- Chen Y, Zhao Y, Zeng L, et al., 2023. Bond performance and bond-slip model for rebar in rubber powder-modified concrete. *Construction and Building Materials*, 375:130934.
- Choi E, Cho BS, Jeon JS, et al., 2014. Bond behavior of steel deformed bars confined by FRP wire jackets. *Construction and Building Materials*, 68:716-725.
- Choi OC, Lee WS, 2002. Interfacial bond analysis of deformed bars to concrete. *ACI Structural Journal*, 99(6):750-756.
- Ferdous W, Manalo A, Siddique R, et al., 2021. Recycling of landfill wastes (tyres, plastics and glass) in construction: A review on global waste generation, performance, application and future opportunities. *Resources, Conservation and Recycling*, 173:105745.
- fib, 2010. *Model Code for Concrete Structures 2010*. Fédération Internationale du Béton, Lausanne.
- Gambarova PG, Rosati GP, 1997. Bond and splitting in bar pull-out: Behavioural laws and concrete cover role. *Magazine of Concrete Research*, 49(179):99-110.
- Ganjian E, Khorami M, Maghsoudi AA, 2009. Scrap-tyre-rubber replacement for aggregate and filler in concrete. *Construction and Building Materials*, 23(5):1828-1836.
- Gao K, Li Z, Zhang J, et al., 2019. Bond behavior between GFRP bars and stirrup-confined concrete. *Applied Sciences*, 9(7):1340.
- GB 50728, 2011. *Technical Code for Safety Appraisal of Engineering Structural Strengthening Materials*. Beijing (in Chineses).
- GB/T 14684, 2011. *Sand for Construction*. Standards Press of China, Beijing (in Chineses).
- GB/T 1499.2, 2007. *Steel for the Reinforcement of Concrete-Part 2: Hot Rolled Ribbed Bars*. Standards Press of China, Beijing (in Chineses).
- GB/T 228.1, 2010. *Metallic Materials-Tensile Testing-Part 1*. Standards Press of China, Beijing (in Chineses).
- Gesoglu M, Güneyisi E, Hansu O, et al., 2015. Influence of waste rubber utilization on fracture and steel-concrete bond strength. *Construction and Building Materials*, 30(101):1113-1121.
- Guo Q, Wang S, Zhang R, 2022. Intrinsic damage characteristics of recycled crumb rubber concrete subjected to uniaxial pressure employing a cohesive zone model. *Construction and Building Materials*, 317:125773.
- Hall MR, Najim KB, 2014. Structural behaviour and durability of steel-reinforced rubberised concrete. *Construction and Building Materials*, 30(73):490-497.
- Huang L, Ye H, Chu S, et al., 2019a. Stochastic damage model for bond stress-slip relationship. *Engineering Structures*, 194:11-25.
- Huang L, Chi Y, Xu L, et al., 2019b. Thermodynamics-based damage-plasticity bond-slip model. *Engineering Structures*, 180:762-778.
- Ka SB, Han SJ, Lee DH, et al., 2018. Bond strength of reinforcing bars considering failure mechanisms. *Engineering Failure Analysis*, 94:327-338.
- Kammash KNA, Al-Quraishi H, Abdul-Husain ZA, 2022. The behavior of bond strength between rebar and concrete in rubberized concrete. *Journal of Engineering*, 28(8):83-92.
- Karunarathna S, Ngo T, Linforth S, et al., 2022. Evaluation of the effect of recycled rubber aggregate size on concrete for sustainable applications in impact-resistant structures. *Journal of Cleaner Production*, 374:133648.
- Li D, Gravina R, Zhuge Y, et al., 2020. Bond behaviour of steel-reinforcing bars in crumb rubber concrete. *Australian Journal of Civil Engineering*, 18(2):2-17.
- Li G, Stubblefield MA, Garrick G, et al., 2004. Development of waste tire modified concrete. *Cement and Concrete Research*, 34(12):2283-2289.
- Li H, Ping K, Chen W, et al., 2024. Bonding performance between steel bar and rubberized concrete under different loading rates. *Journal of Changjiang River Scientific Research Institute*, 41(9):161-168 (in Chineses).
- Li X, Zhao J, Zhang X, 2021. Mechanical bond model for

- reinforcing bars under monotonic and cyclic loading. *Journal of Building Engineering*, 44:102912.
- Liu B, Zhang L, Feng M, et al., 2023. Rubber-concrete-filled CST composite columns under axial compression. *International Journal of Steel Structures*, 23(1):247-262.
- Liu J, Xu W, Li G, et al., 2025. Performance and applications of polymer fiber rubber-reinforced concrete in civil engineering: a state-of-the-art review. *Polymers*, 17(7):970.
- Lu S, Yang J, Wang J, et al., 2024. Steel-tubed rubberized geopolymer concrete columns under axial compression. *Engineering Structures*, 302:117389.
- Mishra S, Panda S, Bhowmik D, et al., 2026. Experimental and analytical evaluation of crumb rubber concrete with multi-blended industrial waste aggregate and SCMs: Strength, durability, microstructure, and ML prediction. *Construction and Building Materials*, 516:145677.
- Pham TM, Chen W, Khan AM, et al., 2020. Dynamic compressive properties of lightweight rubberized concrete. *Construction and Building Materials*, 238:117705.
- Raffoul S, Garcia R, Pilakoutas K, et al., 2016. Optimisation of rubberised concrete with high rubber content: An experimental investigation. *Construction and Building Materials*, 124:391-404.
- Reinhardt HW, Cornelissen HAW, Hordijk DA, 1986. Tensile tests and failure analysis of concrete. *Journal of Structural Engineering*, 112(11):2462-2477.
- RILEM, 1983. RC 6: *Bond test for reinforcement steel-Pull-out test*. RILEM Recommendations.
- Romanazzi V, Leone M, Tondolo F, et al., 2021. Bond strength of rubberized concrete with deformed steel bars. *Construction and Building Materials*, 272:121730.
- Sienkiewicz M, Janik H, Borzędowska-Labuda K, et al., 2017. Environmentally friendly polymer-rubber composites obtained from waste tyres: A review. *Journal of Cleaner Production*, 147:560-571.
- Tang SW, Yao Y, Andrade C, et al., 2015. Recent durability studies on concrete structures. *Cement and Concrete Research*, 78:143-154.
- Tan X, Xing J, Wang Y, et al., 2026. Explainable machine learning for predicting compressive strength of rubberized concrete: SHAP interpretation, lifecycle assessment, and design recommendations. *Journal of Cleaner Production*, 538:147338.
- Topçu IB, 1995. Properties of rubberized concretes. *Cement and Concrete Research*, 25(2):304-310.
- Turatsinze A, Garros M, 2008. Modulus of elasticity and strain capacity of self-compacting concrete incorporating rubber aggregates. *Resources, Conservation and Recycling*, 52(10):1209-1215.
- Velegrakis AF, Ballay A, Poulos S, et al., 2010. European marine aggregates resources: Origins, usage, prospecting and dredging techniques. *Journal of Coastal Research*, 51(6):1-14.
- Wang J, Xiao F, Yang J, 2023. Bond behavior between epoxy-coated reinforcement and seawater sea-sand concrete under FRP-steel confinement. *Construction and Building Materials*, 385:131426.
- Wang J, Xiao F, Yang J, 2024. Bond behavior of stainless steel reinforcement and seawater sea-sand concrete under FRP-steel confinement. *Journal of Materials in Civil Engineering*, 36(3):04023605.
- Wang J, Yang L, Yang J, 2020. Bond behavior of epoxy-coated reinforcing bars with seawater sea-sand concrete. *ACI Structural Journal*, 117(4):193-208.
- Xiao F, Chen S, Chen K, et al., 2025a. Bond behavior of stainless steel rebar to seawater sea-sand concrete: Experiments and modeling. *Engineering Structures*, 330:119960.
- Xiao F, Wang W, Yang J, et al., 2025b. A fractal dimension-modified stochastic damage model for bond-slip responses of corroded steel rebar embedded in different types of geopolymer concrete. *Engineering Structures*, 333:120168.
- Xu Z, Chen S, Qian H, et al., 2023. Analytical bond strength of deformed bars in concrete confined with transverse reinforcement and FRP. *Engineering Structures*, 280:115594.
- Xu Z, Liu Y, Zeng Q, et al., 2022. Improved model for predicting bond strength of rebars with stirrups. *Engineering Fracture Mechanics*, 276:108893.
- Xu Z, Yan D, 2023. Improved prediction for bond strength of FRP-confined concrete. *ACI Materials Journal*, 120(6):19-32.
- Zhang X, Dong W, Lv C, et al., 2019. Analytical modeling of transverse reinforcement effects on bond strength. *Journal of Structural Engineering*, 145(6):04019046.
- Zhang Z, Zhou D, He J, et al., 2023. Insight into the impact of industrial waste co-disposal with MSW on groundwater contamination at open solid waste dumping sites. *Chemosphere*, 344:140429.
- Zhao W, Zhu B, 2018. Theoretical bond-slip model for ribbed steel bars in confined concrete. *Structural Concrete*, 19:548-558

## Electronic supplementary materials

Tables S1, S2, and S3.

## 中文概要

**题目:** FRP-箍筋双重约束下橡胶混凝土与钢筋的粘结性能: 破坏机理与建模

**作者:** 李强<sup>1</sup>, 肖方铎<sup>2</sup>, 卢世伟<sup>3</sup>, 王吉忠<sup>4</sup>, 陈士堃<sup>2</sup>, 闫东明<sup>2</sup>

**机构:** <sup>1</sup>浙江水利水电学院, 建筑工程学院, 中国杭州, 310018; <sup>2</sup>浙江大学, 建筑工程学院, 中国杭

州, 310058;<sup>3</sup>烟台大学, 土木工程学院, 中国烟台, 264005;<sup>4</sup>大连理工大学, 海岸和近海工程国家重点实验室, 中国大连, 116024

**目的:** 本文旨在探讨 FRP/箍筋不同约束条件下, 橡胶混凝土与钢筋的粘结性能, 探究橡胶掺量和约束水平对粘结强度及粘结-滑移响应的影响, 基于试验结果建立粘结性能预测模型。

**创新点:** 1. 基于试验结果, 推导橡胶掺量/约束水平与粘结强度间的定量演化关系; 2. 基于随机损伤理论, 建立粘结-滑移分析模型, 成功模拟橡胶混凝土与钢筋在不同约束条件下的粘结-滑移响应。

**方法:** 1. 通过实验分析, 推导出橡胶掺量和外部约束对粘结强度产生较大的影响 (图 8 和 9); 通过理论推导, 构建粘结-滑移响应的预测模型 (公式 (13) - (17))。

**结论:** 1. 橡胶增多降强度但缓开裂, 40%时破坏模式转优; 2. 约束提升普通混凝土强度, 但对橡胶混凝土效果甚微; 3. 提出粘结强度模型, 揭示高精度及随机非线性特征。

**关键词:** 橡胶混凝土; 橡胶置换率; 粘结强度模型; FRP-箍筋约束; 粘结-滑移模型